DRY-WALL SURVIVAL UNDER IFE CONDITIONS

A. R. RAFFRAY,*† L. EL-GUEBALY,‡ G. FEDERICI,§ D. HAYNES,‖
F. NAJMABADI,# D. PETTI,** and ARIES-IFE TEAM

†*University of California, San Diego, Mechanical and Aerospace Engineering Department and Center for Energy Research, 458 EBU-II, La Jolla, California 92093-0417*
‡*University of Wisconsin, Fusion Technology Institute, 1500 Engineering Drive, Madison, Wisconsin 53706-1687*
§*ITER Garching Joint Work Site, Boltzmannstr. 2, 85748 Garching, Germany*
‖*Los Alamos National Laboratory, MS T085, Los Alamos, New Mexico 87544*
#*University of California, San Diego, Electrical and Computer Engineering Department and Center for Energy Research, 457B EBU-II, La Jolla, California 92093-0417*
**Idaho National Engineering and Environmental Laboratory, Fusion Safety Program, EROB E-3 MS 3815, INEEL, Idaho Falls, Idaho 83415-3815*

Received June 1, 2003
Accepted for Publication April 29, 2004

The chamber wall armor is subject to demanding conditions in inertial fusion energy (IFE) chambers. IFE operation is cyclic in nature, and key issues are (a) chamber evacuation to ensure that after each shot the chamber returns to a quiescent state in preparation for the target injection and the firing of the driver for the subsequent shot and (b) armor lifetime that requires that the armor accommodate the cyclic energy deposition while providing the required lifetime. Armor erosion would impact both of these requirements. Tungsten and carbon are considered as armor for IFE dry-wall chambers based on their high-temperature and high-heat-flux accommodation capabilities. This paper assesses the requirements on armor imposed by the operating conditions in IFE, including energy deposition density, time of deposition, and frequencies; describes their impact on the performance of the candidate armor materials; and discusses the major issues.

KEYWORDS: *inertial fusion energy, dry chamber wall, photon and ion energy deposition*

I. INTRODUCTION

Inertial fusion energy (IFE) operation is cyclic in nature, and the power plant chamber wall must accommodate the cyclic and intense photon and ion energy deposition while providing the required lifetime. This is a particular demanding requirement for the dry chamber wall configuration. Past studies, such as SOMBRERO,[1] indicated the need for a protective gas at a significant pressure (e.g., xenon at ~0.1 to 0.5 torr) to prevent unacceptable wall erosion for a carbon chamber wall even for direct-drive targets. This created a formidable challenge for such a design since the presence of a gas would also have to accommodate target and driver requirements. Only a minimal target temperature increase (order of 1 K) can be tolerated during injection to maintain the required target uniformity for a symmetrical burn. High-speed target injection (approximately hundreds of meters per second) through a background gas could result in higher target temperature deviation because of heat transfer from the gas. The presence of a background gas could also lead to laser breakdown depending on the gas density. Until recently, no reasonable design window seemed to exist that satisfied the conflicting chamber gas constraints from wall protection on one hand and from target and driver considerations on the other.

A recent effort as part of the ARIES-IFE program has provided a more detailed assessment of the dry chamber wall. Several material options were considered including a carbon and tungsten flat wall and a high-porosity fibrous carbon configuration to maximize the incident surface area and help accommodate the energy deposition. The goal was to better understand the operating design windows based on armor lifetime and on target and driver requirements and to characterize the key issues.

Both direct-drive- and indirect-drive-target cases were considered as part of the ARIES-IFE studies. The

*E-mail: raffray@fusion.ucsd.edu

indirect-drive-target pellet is contained within a relatively massive hohlraum enclosure that after the microexplosion would result in much more demanding conditions on the wall in terms of X rays and target debris fluxes. Given the challenge for a dry-wall configuration to accommodate the threats even from the less demanding direct-drive target, the studies were focused mainly on this latter case and so are the results reported here. A direct-drive target is often coupled with a laser that is also the main example driver considered here.

The results of the ARIES-IFE dry-wall studies are described in this paper. First, the threat spectra of the example targets considered are described, and the energy deposition calculations are highlighted. Next, the materials considered are discussed. The wall thermal analysis modeling is then described, and the results are highlighted and discussed. Key issues are discussed with the aim of helping to guide research and development (R&D) effort and to highlight possible synergies with R&D for plasma-facing components (PFCs) in magnetic fusion energy (MFE). Larger issues linked with the choice of a dry-wall armored chamber must also be considered when developing such a configuration. As an illustration, two such issues are also discussed: the activation issues linked with disposal of target materials and an example safety analysis for an air ingress scenario.

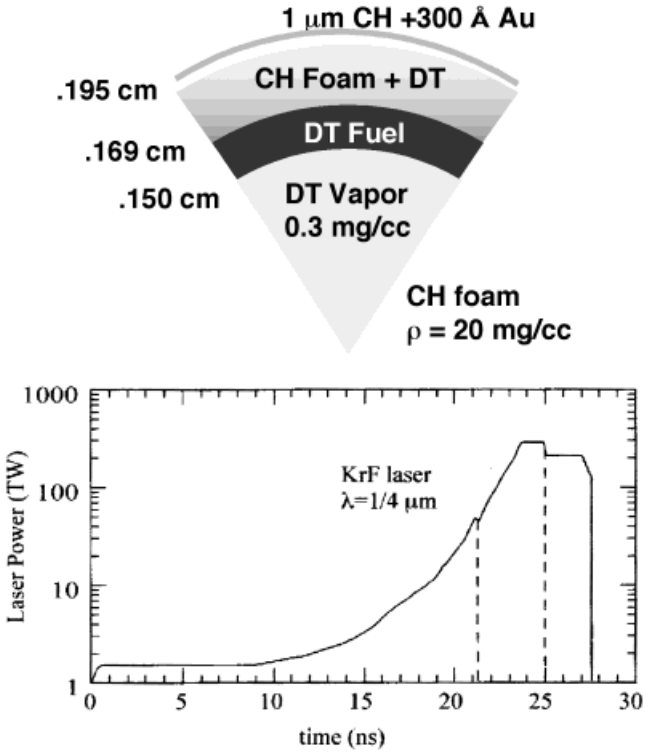

Fig. 1. Example direct-drive target (NRL) to be coupled with a laser driver.[2,3]

II. TARGET SPECTRA

Two different kinds of targets were considered:

1. a direct-drive target, illustrated in Fig. 1, whereby the driver energy is deposited directly on the target
2. an indirect-drive target utilizing a radiation hohlraum enclosure. The X rays resulting from the driver beam interaction with the hohlraum material are then deposited on the deuterium-tritium (D-T) target pellet inside the hohlraum. Such an option has been considered in particular in conjunction with a heavy-ion-beam driver.

The energy partitioning from the two example direct-drive and indirect-drive targets [a 154-MJ Naval Research Laboratory (NRL) laser direct-drive target[2,3] and a 458-MJ heavy-ion indirect-drive target[4,5]] are shown in Table I based on LASNEX calculations.[4] The photons and ions are the major threats to the chamber wall. Neutrons penetrate much more deeply into the structure and blanket and as such are much less of a threat to the chamber wall. The corresponding photon spectra for both targets are shown in Fig. 2. The major difference between the direct-drive and indirect-drive threat spectra is the huge energy component carried by photons in the indirect-drive case (25%) as opposed to the direct-drive case (1%), albeit with a softer spectrum. The photon energy deposition time is very small (typically subnanoseconds), which results in large heat fluxes and makes it very challenging for a wall to accommodate the indirect-drive-target photon threat. Consequently, although results presented in this paper cover both the direct-drive- and indirect-drive-target cases, there is more of a focus on the direct-drive-target case. The burn products (fast ions) and debris ion spectra for the 154-MJ direct-drive target are shown in Figs. 3 and 4, respectively. A recently proposed higher-yield direct-drive target (~401 MJ) with similar relative energy partitioning and threat spectra as the 154-MJ case was also considered. More detailed information on the ion spectra for both direct-drive targets (154 and 401 MJ) as well as for the 458-MJ indirect-drive target can be found in Ref. 4.

III. CANDIDATE DRY-WALL ARMOR CONFIGURATIONS AND MATERIALS

Candidate dry chamber armor materials must have high-temperature capability and good thermal properties to accommodate energy deposition and provide the required lifetime. Processes affecting armor lifetime include erosion and local armor failure. Ablated material must also be considered in the chamber clearing process

TABLE I

Energy Partitioning for 154-MJ NRL Direct-Drive Target and 458-MJ Heavy-Ion Indirect-Drive Target

	NRL Direct-Drive Target (MJ)	Heavy-Ion Indirect-Drive Target (MJ)
X rays	2.10 (1.4%)	115 (25%)
Neutrons	109 (71%)	316 (69%)
Gammas	0.0089 (0.006%)	0.36 (0.1%)
Burn product fast ions	19.5 (13%)	8.43 (2%)
Debris ion kinetic energy	22.1 (14%)	18.1 (4%)
Residual energy	1.29	0.57
Total	154	458

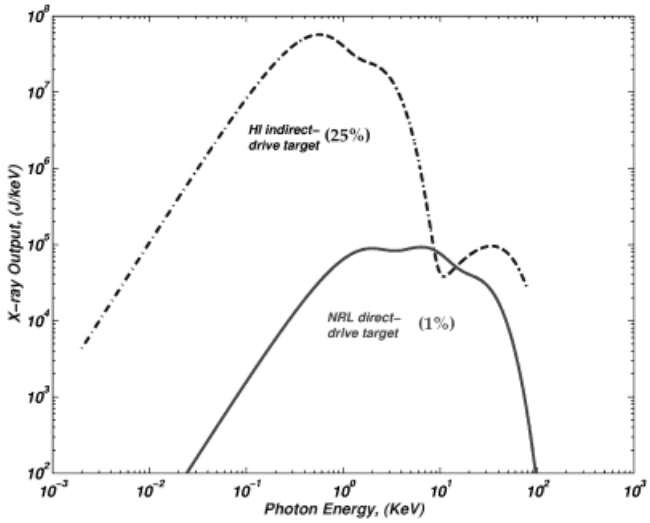

Fig. 2. Photon spectra from NRL 154-MJ direct-drive target and 458-MJ heavy-ion-beam indirect-drive target.[4]

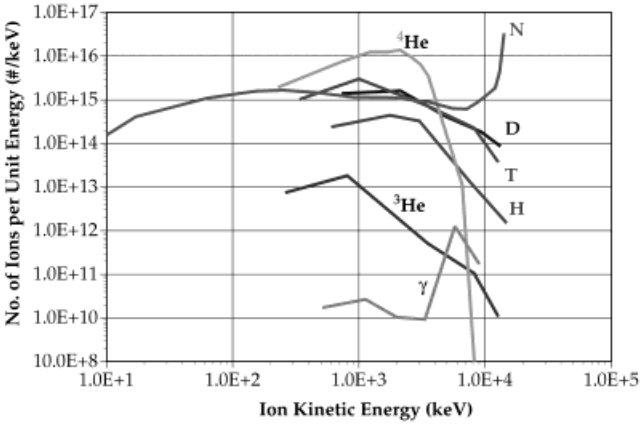

Fig. 3. Fast ion spectra from NRL 154-MJ direct-drive target.[4]

to ensure that after each shot the chamber returns to a quiescent state in preparation for the target injection and the firing of the driver for the subsequent shot. Carbon that shows good high-temperature resistance and thermal properties was the major candidate armor considered in past studies (e.g., Ref. 1). However, several mass loss processes have been identified in carbon including chemical erosion and radiation-enhanced sublimation that lead to key concerns of lifetime and tritium inventory through codeposition in cold regions, as will be discussed in Sec. VI.C. In this regard, refractory metals, such as tungsten, are attractive candidates since they also offer good high-temperature capability but without the tritium codeposition and inventory concern. However, melting can be an issue for severe energy deposition scenarios depending on the stability of the melt layer and on the form of the resolidified material. Both carbon and tungsten are currently considered as armor material candidates for IFE. In addition, the possibility of utilizing an engineered surface [such as a high-porosity fibrous carpet, illustrated in Fig. 5 (Ref. 6)] to maximize the incident area and provide better accommodation of high-energy deposition is being investigated. Typical carbon and tungsten thermophysical properties are listed in Table II.

IV. ENERGY DEPOSITION IN DRY WALL FROM TARGET SPECTRA

The energy deposition in the material was calculated based on the photon and ion spectra for the corresponding targets. A one-dimensional (1-D) slab geometry was assumed, and the calculations were performed for carbon and tungsten. An attenuation calculation was used for the photon energy deposition based on data for the attenuation coefficient in the material (including photoelectric and Compton scattering effects) as a function of the photon energy.[13] The ion deposition calculation included both the electronic and nuclear stopping powers that were obtained as a function of ion energy from SRIM (Ref. 14).

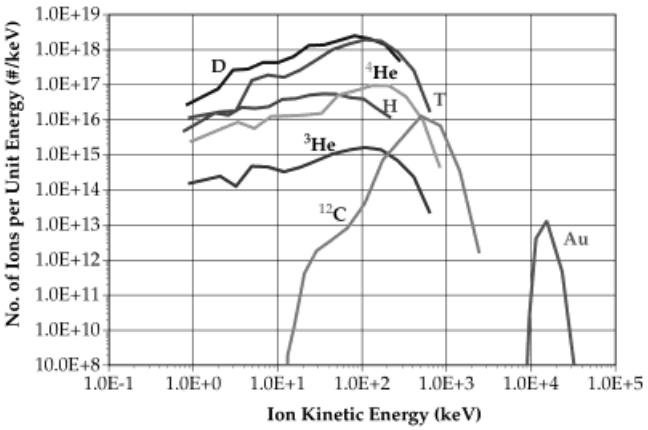

Fig. 4. Debris ion spectra from NRL 154-MJ direct-drive target.[4]

The calculations proceeded by following ions at discretized energy levels from the spectra through the material slab. Figure 6 shows the energy deposition as a function of penetration depth for carbon and tungsten for the 154-MJ direct-drive target spectra assuming a chamber radius of 6.5 m and no protective gas in the chamber. A similar plot for the 401-MJ direct-drive target spectra is shown in Fig. 7.

The calculation procedure included the time-of-flight spreading of the photon and ion energy deposition. The photons travel much faster than the ions and would reach the chamber wall within ~20 ns over a time spread of subnanoseconds. The ions take longer to reach the chamber wall and would reach the wall at different times depending on their energy, thereby spreading the energy deposition over time and lowering the heat flux seen by the wall. As an example, a simple estimate of the ion time of flight based on kinetic energy is shown in Fig. 8 for the 154-MJ direct-drive target spectra for a case without any protective gas in a chamber of radius 6.5 m. The fast ions reach the wall within ~0.2 to 1 μs whereas the slow ions reach the wall within 1 to 2.5 μs.

V. THERMAL ANALYSES

The thermal analysis was carried out using a 1-D code based on RACLETTE (Ref. 9) including melting and evaporation, and using BUCKY (Ref. 15), an integrated 1-D code that calculates the photon and ion energy deposition and the wall thermal response for cases with and without a protective gas. Temperature-dependent properties were utilized for both carbon and tungsten; the thermal conductivity of carbon tends to decrease appreciably with neutron irradiation, and the thermal

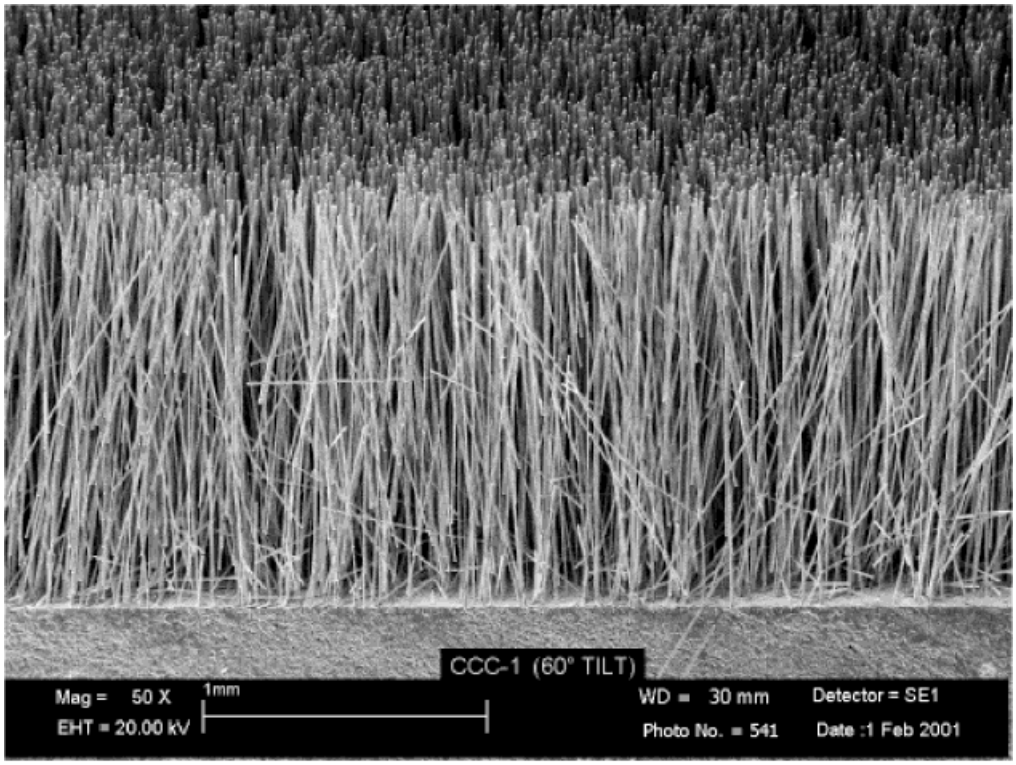

Fig. 5. ESLI carbon fibrous carpet.[6]

TABLE II

Summary of Main Armor Material Properties

Thermophysical Properties	Tungsten	Carbon[a]
Density (kg/m^3)	~19 350 (Ref. 7)	~2000 (Ref. 8)
Phase change temperature, T_{pc} (K)	3683 (Ref. 7) (melting)	3640 (Ref. 9) (sublimation)
Thermal conductivity, k (W/m·K)	148 (500 K) (Refs. 7 and 8) 90 (3000 K) (Ref. 8)	90 (573 K)[b] (Ref. 10) 213 (>1500 K) (Ref. 10)
Specific heat, C_p (J/kg·K)	138 (500 K) (Ref. 8) 225 (3000 K) (Ref. 8)	1350 (500 K) (Ref. 7) 2450 (3000 K) (Ref. 7)
Heat of fusion, h_{fg} (kJ/kg)	192 (Ref. 7)	—
Heat of vaporization, h_v (kJ/kg)	4009 (Ref. 7)	59 400[c] (Refs. 9 and 11)
Molecular weight	183.85 (Ref. 8)	12
Parameters in vapor pressure Eq. (2) (K)		
A_i	12.74 (Refs. 9 and 12)	15.75 (Ref. 11)
B_i	44 485 (Refs. 9 and 12)	40 750 (Ref. 11)
Assumed condensation coefficient, σ	~1	0.12 (Ref. 11)

[a]A thin vapor deposition carbon armor is assumed over a carbon-fiber-composite structure.
[b]Thermal conductivity of neutron-irradiated MKC-1PH carbon-fiber composite (1 dpa).
[c]This value is based on sublimation of monoatomic carbon C_1 and is used in the example calculations presented in this paper. However, this value will change depending on the molecular form and distribution of sublimated carbon (i.e., C_2, C_3 or even $C_{4,5}$ molecular clusters). This is an important issue that must be considered in more detailed calculations.[11]

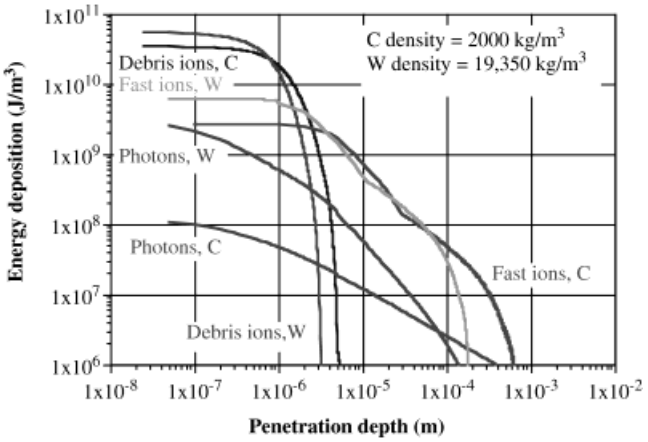

Fig. 6. Energy deposition as a function of penetration depth for carbon and tungsten for the 154-MJ direct-drive target spectra assuming a chamber radius of 6.5 m and no protective gas in the chamber.

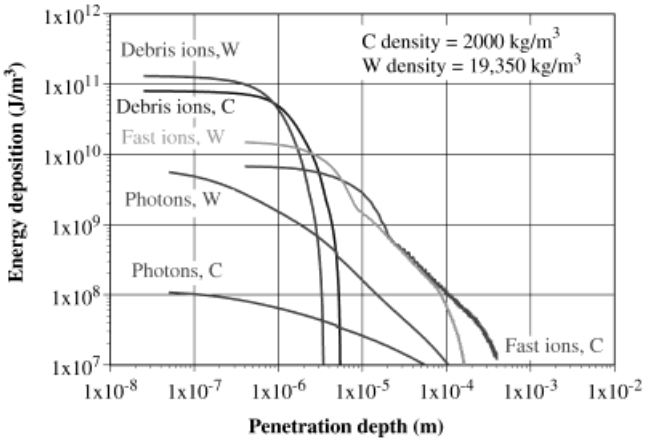

Fig. 7. Energy deposition as a function of penetration depth for carbon and tungsten for the 401-MJ direct-drive target spectra assuming a chamber radius of 6.5 m and no protective gas in the chamber.

conductivity data for irradiated carbon (1 dpa) were used. Typical properties are shown in Table II.

V.A. Armor Analysis for Cases Without a Chamber Gas

Calculations for the case with no protective chamber gas were performed using the modified RACLETTE code. Melting was modeled by changing the enthalpy of the material over ~1 K at the melting point to account for the latent heat of fusion. Evaporation or sublimation was modeled by calculating the evaporated flux as a function of the wall temperature and then multiplying by the latent heat of evaporation to calculate the effective heat flux, as described below.

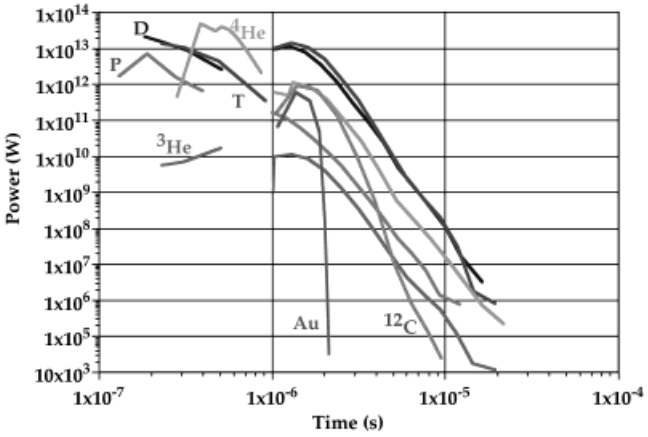

Fig. 8. Ion power deposition as a function of time for 154-MJ NRL direct-drive target.

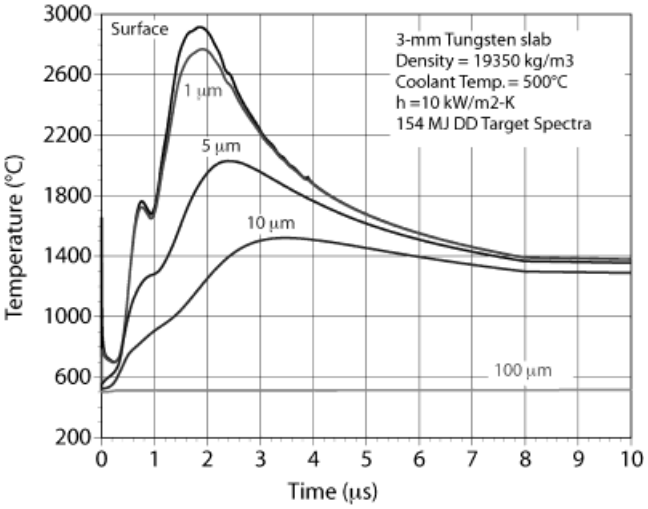

Fig. 9. Temperature history at different locations in a 3-mm tungsten slab without a protective gas exposed to the 154-MJ direct-drive-target threat spectra in a chamber of radius 6.5 m and with a coolant temperature of 500°C.

Under the assumption that at equilibrium the condensation heat flux based on the vapor pressure and temperature would be equal to the evaporation flux based on the wall temperature, the latter can be estimated as follows:

$$G = \sqrt{\frac{M}{2\pi RT}}\,\sigma P_{vap} \quad , \tag{1}$$

where

G = evaporated mass flux (kg/m^2·s)

M = molecular weight

R = gas constant (J/kmol·K)

σ = condensation coefficient

P_{vap} = vapor pressure (Pa) corresponding to the armor surface temperature typically given by

$$\log P_{vap} = A_i - \frac{B_i}{T} \quad . \tag{2}$$

Multiplying G by the latent heat of vaporization h_v (in joules per kilogram) yields the evaporation heat flux as a function of the surface temperature. The values of these different parameters used in the analysis for carbon and tungsten can be found in Table II.

Example results for a 3-mm tungsten slab without a protective chamber gas are shown in Fig. 9 for a chamber radius of 6.5 m and a coolant temperature of 500°C. The major observations emerging from the results include the following:

1. The photon energy deposition is very fast and creates an instantaneous temperature increase of ~1150°C.

2. The maximum tungsten temperature is <3000°C. It is not clear whether total melt avoidance would be required as this would depend on the stability of the melt layer and on the material form and integrity following resolidification. However, even assuming a melting point limit (3410°C), the results indicate some margin for adjustment of parameters such as target yield, chamber size, coolant temperature, and protective gas pressure.

3. All the action takes place in a very thin region (<100 μm) based on which a design with separate functions is preferred: a thin armor providing the high-energy accommodation function bonded to a structural substrate providing the structural function and interfacing with the blanket that effectively sees quasi-steady-state conditions.

Figure 10 shows the results for a carbon armor case. Generally, the observations are the same as for the tungsten case except that the initial photon-induced peak is much smaller since the photon energy deposition goes more deeply inside the carbon and the maximum temperature is <2000°C with an associated annual sublimation loss of <1 μm. From these results, a carbon wall can survive the photon and ion energy deposition from this target even without gas protection with some margin to allow for design optimization on various parameters.

Calculations done for the 401-MJ direct-drive-target case in the absence of any protective gas showed unacceptable melting and evaporation in the case of tungsten and unacceptable sublimation in the case of carbon, indicating the need for a protective chamber gas for chamber sizes of ~6.5 m in radius. For example, for such a chamber size with a coolant temperature of 500°C, the calculations indicated a maximum tungsten temperature of ~6800°C with a corresponding melt layer of ~7.3 μm and evaporation loss of ~0.08 μm per shot. For carbon, the maximum temperature was calculated as ~4100°C with a corresponding sublimation loss thickness of

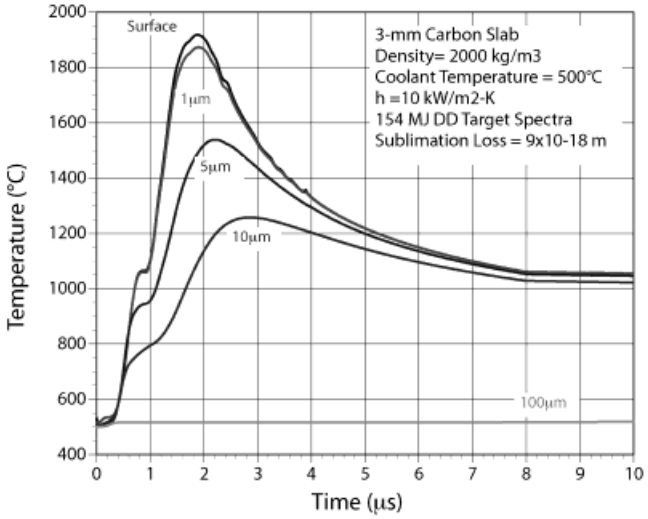

Fig. 10. Temperature history at different locations in a 3-mm carbon slab without a protective gas exposed to the 154-MJ direct-drive-target threat spectra in a chamber of radius 6.5 m and with a coolant temperature of 500°C.

0.06 μm per shot (which, for a repetition rate of 10, corresponds to ~50 mm/day of armor loss).

Calculations were also performed to help understand the advantages provided by an engineered surface in accommodating high incident heat fluxes as compared to a flat surface. Recent results from experiments with the RHEPP ion source indicated superior performance from a high-porosity carbon fiber carpet (illustrated in Fig. 5) as compared to a flat carbon surface.[16] The ion sources were carbon and hydrogen at ~200 to 300 keV with fluences at the armor surface of ~5 J/cm^2. It is recognized that a key issue associated with this particular carbon fibrous carpet is the large carbon surface area that could lead to carbon ablation of some sort (e.g., shallow angle sputtering along the fiber length although the sputtered carbon atoms might redeposit on adjacent fibers) and tritium codeposition in colder regions. This overall issue must be studied in more detail for prototypical conditions, and possible solutions such as coating the fiber with a thin tungsten layer or manufacturing a similar carpet from tungsten filaments should be investigated. For the scope of this paper, thermal analyses were performed to help understand the performance of such a fibrous concept from a purely heat flux accommodation basis with the understanding that such a concept will have to be further improved for IFE armor application.

The high-porosity carpet is made of high-aspect-ratio fibers (~2 to 3 mm long, 5 to 10 μm in diameter, with overall carpet porosity ~96 to 99%). A simple model was developed for the thermal analysis of this fibrous carpet, as illustrated in Fig. 11. First, the fibers of diameter d were assumed to be placed in a square pattern with separation distance y, estimated from the porosity. A simple probability function was assumed whereby the probability of an incident ion flux to hit a fiber in the first incident plane of fibers is estimated as (d/y). The probability of the incident ion flux to hit a fiber in the second plane of fibers is $\{(1 - d/y)([d/(y - d)]\}$, and so on. In this way, a simple estimate of the effective distance between fibers y_{eff} could be obtained by adding the product

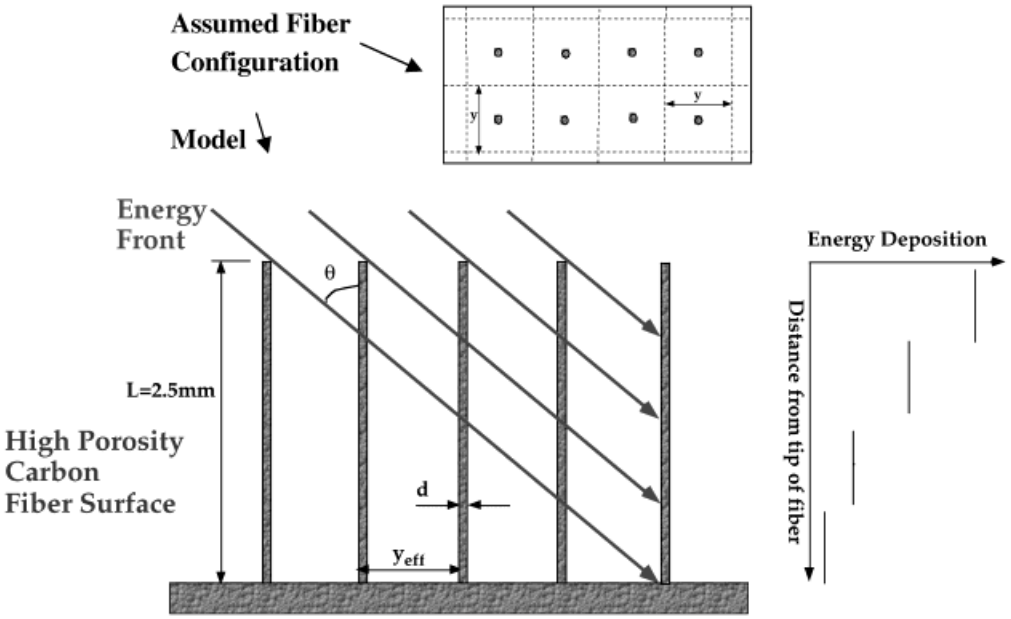

Fig. 11. Schematic of fibrous carpet modeling.

TABLE III

Parameters of Example Fibrous Carpet Analyzed and Summary of Results for Different Incidence Angles

Fiber Characteristics			
	Length, L	2.5 mm	
	Diameter, d	6.5 μm	
	Volume fraction	1.5%	
	Separation, y	47 μm	
	Effective separation, y_{eff}	215 μm	
Incidence Angle (deg)	Maximum Fiber Temperature (°C)	Average Fractional Sublimation Loss at Single Fiber Tip[a]	Overall Fractional Sublimation Loss of Fibrous Carpet
0	4390	1	0.015
5.2	4352	0.43	0.0065
10	4292	0.31	0.0046
20	4213	0.15	0.0023

[a]Fractional sublimation loss of 1 is equivalent to ~0.032 μm per shot.

of distance and probability linked to each plane of fibers. This was used in developing the final model geometry shown in Fig. 11. The ion energy deposition in one example fiber was calculated for a given incidence angle θ by taking into account the shadowing effect of fibers in all previous incident planes. A two-dimensional ANSYS model was then used to perform the transient thermal analysis of this example fiber under the given ion energy deposition including also time-of-flight effects associated with the ion energy spectra. The results are summarized in Table III. For this example fibrous carpet case, the incident angle to prevent shine-through of the ions to the substrate is ~1 deg based on the fiber separation distance y and ~5 deg based on y_{eff}.

The sublimation loss per fiber is based on the temperature distribution at the tip. At a 0-deg incidence angle, this is equivalent to a flat carbon surface that is the normalization factor used for the sublimation values shown in Table III. The angle of incidence does help to some extent in reducing the maximum fiber temperature and the sublimation loss as compared to the flat case. However, the major effect is associated with the very low fiber density (0.015) that correspondingly reduces the overall fractional sublimation. These results are in agreement with postexperimental examination of fibers following the RHEPP shot, which showed no visible ablation or loss of material. These results confirm the advantages associated with the engineered surface, offering the possibility of reducing the maximum temperature to some extent and minimizing any ablation.

V.B. Armor Analysis for Cases with a Chamber Gas

Use of a background chamber gas has been widely considered to protect the chamber armor from the cyclic threat of high-energy photons and ions in order to achieve the desired armor lifetime. However, the chamber gas conditions must satisfy target and driver constraints prior to each shot. The chamber gas provides a medium that absorbs the target X rays and ions and reemits the energy over a timescale sufficiently long that the permanent target chamber structures can cope with the insult. This section details results from the simulation of dry-wall chambers protected by a buffer gas based on the BUCKY code.

A buffer gas in the target chamber absorbs some of the target X rays and ions, reemitting the absorbed energy through one of two processes. Photons from the relaxation of excited electrons through bremsstrahlung, radiative recombination, or photodeexcitation are emitted at rates determined by the emission opacity of the gas. Some of the absorbed energy is thermalized, and the gas conducts the heat to the wall through conduction. The effect of these processes is to further stretch the timescales associated with the insult to the wall in addition to the effect of the time-of-flight spreading. This mitigation of the insult to the first wall affords an opportunity to reduce the chamber radius and/or to increase the first-wall operating temperature. The effects of the chamber gas on driver beam propagation, target injection, and target heating must be considered and will be discussed in the following sections.

Xenon has been considered as a protective chamber gas in previous studies based on its combination of chemical inertness and opacity. For example, in the SOMBRERO reactor design,[1] xenon at 0.5 torr (conventionally used to represent the gas density at a temperature of 300 K) was proposed to protect the graphite first wall from the 22 MJ of X rays and 84 MJ of ions emitted by the ignited target. The opacity of the xenon gas depends

on the population of the energy levels of its various ionization stages. For the low-density high-temperature conditions in the blast wave, the ionization balance of xenon is far from that of collisional equilibrium, and a collisional-radiative equilibrium population kinetics code, IONMIX, is used to generate the xenon equation of state and opacity. IONMIX takes as input the ionization potentials of all of the ionization stages of the plasma constituents and assumes screened hydrogenic atomic physics (excitation energies, ionization potentials, and atomic rates) for the excited states in the solution of the equations of collisional-radiative equilibrium. Note that the local thermal equilibrium approximation would significantly overestimate the ionization of the xenon, enhancing the rate of reemission and, thus, is not appropriate for the calculation of chamber gas reaction for the gas densities considered for chamber protection.

BUCKY, a 1-D Lagrangian radiative-hydrodynamics code,[15] is used for the simulation of the response of the buffer gas and armor to target X-ray and ion threat spectra. Prompt X-ray deposition is modeled using cold opacities from Biggs and Lighthill. Deposition of ion energy is approximated by the theory of Melhorn,[17] and the free electron contribution interpolates between the low-energy Lindhard-Scharff limit and the high-energy Bethe limit. Radiation transport[18] is calculated in the flux-limited multigroup diffusion approximation. Energy that reaches the wall is treated as a source term in a thermal diffusion equation. As the temperature in a wall cell approaches the vaporization temperature, the zone begins to vaporize at a rate determined by the relative rates of vaporization and condensation, as determined by the kinetic theory of Labuntsov and Kryukov.[19]

The amount of xenon required to prevent unacceptable mass loss per shot depends on the yield of the target as well as the partitioning and spectra of the nonneutronic components of target output. This is illustrated in Fig. 12 for three different target outputs in substantially similar tungsten armored chambers. Two of the targets (ID1, the 458-MJ indirectly driven heavy-ion-beam target, and DDHY, the 401-MJ high-yield directly driven laser target) have similar yields but substantially different threat partitioning and spectra, as discussed above. The two direct-drive targets have similar threat partitioning and spectra but substantially different yields (400 MJ for DDHY and 154 MJ for DDLY). The indirectly driven target requires by far the most xenon to prevent wall loss because its threat is dominated by shallowly penetrating soft X rays (~1 keV) that are not affected by time-of-flight spreading. The direct-drive target with similar yield requires only 1/20th the amount of xenon to prevent wall loss because its threat spectrum is dominated by debris ions whose threat is substantially reduced by time-of-flight spreading. For all three cases, the high-energy burn product ions implant into the wall, and the effect of this implantation on the long-term material properties of the armor is an active area of research.

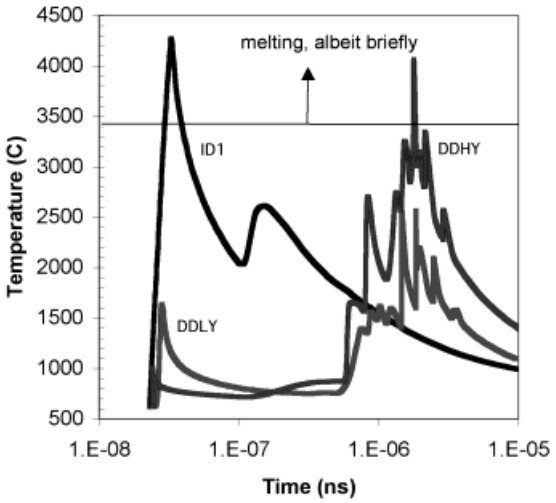

Fig. 12. Thermal response of the surface of a tungsten-coated xenon-buffered dry-wall IFE chamber to the threats from three different IFE targets. The curve labeled ID1 is for the 458-MJ indirectly driven heavy-ion-beam target in a 6.9-m-radius chamber. Those labeled DDLY and DDHY are for the low-yield (154-MJ) and high-yield (401-MJ) directly driven laser targets, respectively, in a 7.2-m-radius chamber. The xenon pressures for the calculations are for ID1, 500 mtorr; DDLY, 10 mtorr; and DDHY, 28 mtorr, where the convention is to quote densities in pressure equivalents at 330 K, or 1 torr = $3.54 \times 10^{16}/\text{cm}^3$).

An operating window for armor thermal behavior can be evolved by setting an allowable ablation thickness per shot. For example, for the 154-MJ direct-drive target spectra and a 6.5-m chamber with carbon armor, Fig. 13 shows the combinations of protective gas density and wall temperature that would result in one monolayer (~2 Å) per shot of sublimated wall material. These results are shown as an illustration as it is recognized that loss of even one atomic monolayer (~2 Å) per shot would result in unacceptably high annual armor erosion (approximately centimeters) and that a more severe constraint has to be set (e.g., assuming that so many atoms are lost per shot corresponding to a uniform average loss of a fraction of a monolayer). From Fig. 13 the thermal operating window is quite large. However, the overall operating window is substantially reduced when including constraints arising from target and driver considerations, as discussed in Ref. 20.

The operating window for armor thermal behavior would be shifted toward higher gas densities for an indirect-drive-target case where the large fraction of energy emitted as soft X rays necessitates the presence of a substantially denser gas for this chamber design. This is illustrated in Fig. 13, which also shows the combinations of protective gas density and wall temperature that would result in one monolayer per shot of sublimated

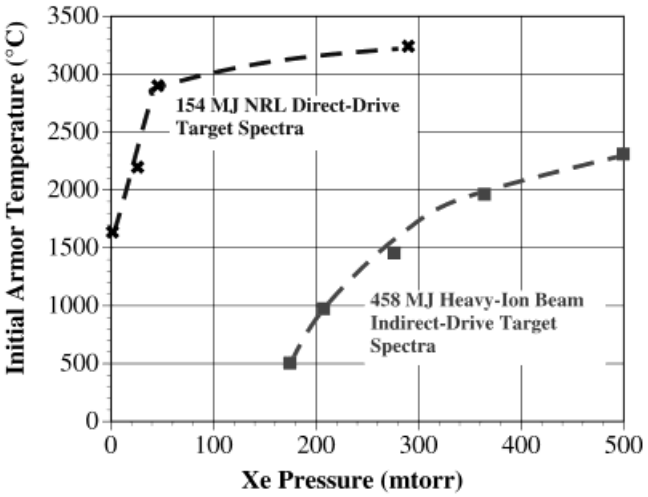

Fig. 13. Example operating window for the thermal behavior of a chamber of 6.5-m radius with carbon armor and xenon as protective gas for the 154-MJ direct-drive-target case and the 458-MJ indirect-drive-target case (lines connecting the points are present to guide the eye).

wall material for the 458-MJ heavy-ion-beam indirect-drive-target case. Target injection and heating complications associated with the presence of the buffer gas are of much less concern for the massive, thermally shielded indirectly driven heavy-ion-beam target. Constraints from driver requirements would tend to be more restrictive on the maximum allowable gas density.[20]

The possibility of using helium as protective gas was investigated. Helium is created as a product of the reaction, and using it also as a buffer gas would reduce the number of species in the chamber. However, the results showed that a much higher helium density would be required for wall protection as compared to xenon. This can be explained by the lower number of electrons available per gas atom to be stripped and becoming highly efficient components in the slowing of debris ions. To be as effective as xenon in stopping ions, any gas atom or molecule, after the X-ray flash to the plasma, should be capable of yielding at least approximately ten electrons that will then slow the ions.

VI. MAJOR ARMOR ISSUES

Although the base operating conditions of IFE (cyclic operation) and MFE (with the goal of steady-state operation) are fundamentally different, an interesting parallel can be drawn between armor conditions under IFE and some MFE dynamic scenarios. For example, as shown in Table IV, the frequency, energy density, and particle fluxes on the ITER divertor associated with Type 1 edge-localized-mode (ELM) scenarios are within about one

TABLE IV
Conditions Assumed for ITER ELM Scenarios, Vertical Displacement Events, and Disruptions Compared to Conditions Associated with a Typical Direct-Drive-Target IFE (NRL 154-MJ Target)*

	ITER Type-I ELMs	ITER Vertical Displacement Events	ITER Disruption Thermal Quench	Typical IFE Operation (154-MJ Direct-Drive NRL Target)
Energy	10 to 12 MJ	~50 MJ/m^2	100 to 350 MJ	~0.1 MJ/m^2
Affected area	5 to 10 m^2[a]	A few square meters[a]	~10 m^2[a]	Chamber wall ($R \sim 5$ to 10 m)
Location	Surface (near divertor strike points)	Surface/bulk	Surface (near divertor strike points)	Bulk (approximately microns)
Time	≥200 μs	~0.3 s	~1 ms	~1 to 3 μs
Maximum temperature	Melting/sublimation	Melting/sublimation	Melting/sublimation	~2000 to 3000°C (for dry wall)
Frequency	Few hertz	~1 per 100 cycles	~1 per 10 cycles	~10 Hz
Base temperature	≥500°C	~200°C	200 to 1000°C	Approximately >700°C
Particle fluxes	~10^{24} m$^{-2}\cdot$s^{-1} (peak under normal operation)			~10^{23} m$^{-2}\cdot$s^{-1}

*From Ref. 21.
[a]Large uncertainties exist.

order of magnitude of those for IFE (Ref. 21). Consequently and interestingly, issues driving the choice of armor material tend to be similar for MFE and IFE, which provides the possibility of synergy when planning and carrying out supporting R&D. On the IFE side, much of the dry-wall R&D effort is being carried out as part of the High-Average-Power-Laser Program involving several research institutions and led by the NRL (Ref. 22).

The dry-wall armor issues are broadly linked with armor performance, lifetime, safety, and fabrication and are discussed below.

VI.A. Microscopic Erosion

Erosion directly impacts armor lifetime. Ablated material must also be considered in the chamber clearing process to ensure that after each shot the chamber returns to a quiescent state in preparation for the target injection and the firing of the driver for the subsequent shot. Furthermore, from MFE experience, carbon erosion can lead to large tritium inventory through codeposition with tritium in cold regions, as will be discussed in Sec. VI.C. In addition to vaporization and sublimation included in the analysis presented in Sec. IV, microscopic and macroscopic erosion mechanisms could influence armor lifetime. Macroscopic mechanisms tend to arise from local stresses or from melting and result in chunks or droplets of material being injected, which is discussed as part of Sec. VI.B. Microscopic processes include physical sputtering and, in the case of carbon, chemical sputtering and radiation-enhanced sublimation (RES). These have been studied for many years in the context of MFE, and good progress has been made in understanding the underlying physical processes. A detailed and comprehensive review of these erosion mechanisms and other issues for MFE plasma material can be found in Ref. 23. In light of such information, these mechanisms are assessed and discussed below in the context of IFE. Note that implantation and accumulation of ions (in particular of helium ions in tungsten) leading to possible blistering or armor failure represent an additional erosion mechanism, which is discussed separately as part of the effects of irradiation in Sec. VI.D.

A fairly complete theory of physical sputtering now exists. Importantly, the predicted sputtering yields, as well as the expected trends with species properties (e.g., atomic mass, surface binding energy), have been experimentally verified in both tokamaks and laboratory devices.[24,25] For plasma-facing materials, including beryllium, carbon, and tungsten, erosion data exist for hydrogen, deuterium, and helium in the energy range from 10 eV up to 10 keV (Refs. 26 and 27). The data are extended to higher energies and to tritium by computer simulation.[27,28] At grazing incidence the erosion yield is enhanced relative to the yield at normal incidence, as more energy is deposited within the near-surface layer. Surface roughness tends to reduce the pronounced dependence of the sputtering yield on the angle of incidence. Physical sputtering of pure elements at relatively low temperature is well understood and can be simulated with computer codes.[29] However, recent investigations on metals such as lithium and gallium show an increase of the erosion rates, and a dependence of the yield on the incidence flux, for a broad range of temperatures near the melting point. For beryllium, tungsten, and carbon, experimental data and the fit for the sputtering yield at normal incidence are shown in Fig. 14 for deuterium ions as a function of incident particle energy. For carbon, the curves for physical sputtering with deuterium ions are taken from computer simulations and are compared to experimental data, which include chemical effects (hence the poor fit). It is interesting to see that the carbon physical sputtering yield peaks at a value of ~0.03 for deuterium ion energies of approximately hundreds of electronvolts. For tungsten, there is a threshold ion energy of ~1 keV beyond which the physical sputtering yield increases sharply and then tends to peak at a value of ~0.006 for ion energies of ~10 keV. As shown in Figs. 3 and 4, the deuterium and tritium ion energy from the direct-drive target spectra are well above these values.

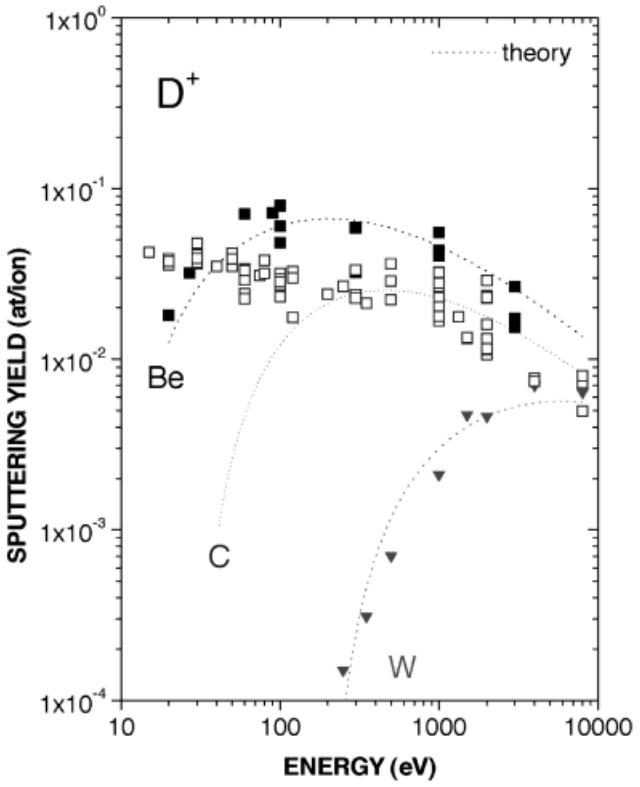

Fig. 14. Comparison of measured values for the sputtering yield at normalized incidence for beryllium (closed squares), carbon (open squares), and tungsten (closed triangles) by deuterium ions with results from analytical modeling of physical sputtering.

However, depending on the density of the protective gas used in the chamber, the ion energies could be attenuated to these levels. A simple estimate of sputtering from a chamber wall can be made from the following expression:

$$\delta = \frac{IY_i M_i}{10^3 N_0 \rho_i 4\pi R^2} \quad , \tag{3}$$

where

δ = armor loss per shot (m)

I = number of incident ions per shot

Y_i = sputtering yield (atom/ion)

M_i = armor molecular weight

N_0 = Avogadro's constant

ρ_i = armor density (kg/m^3)

R = chamber radius (m).

For the direct-drive target spectra shown in Figs. 3 and 4, >90% of the incident ions are hydrogen species; the rest consist mostly of helium species. These are light ions, and it seems reasonable to use the sputtering results for deuterium ions to provide a rough estimate of what to expect in such an IFE situation. For a chamber of radius $R = 6.5$ m, with $I = 10^{21}$ ions/shot consistent with the 154-MJ direct-drive target spectra (see Figs. 3 and 4), the loss per shot for carbon and tungsten are 5.6×10^{-13} m and 1.9×10^{-13} m for the respective maximum physical sputtering yield values of 0.03 and 0.006. For operation at a repetition rate of ~10, these values would translate to an annual armor loss of 0.18 and 0.06 mm for carbon and tungsten, respectively. These values are clearly acceptable, and this simple estimate suggests that sputtering yield would not be a major issue for IFE.

For carbon, chemical reactions with incident hydrogen ions are also possible, leading to the formation of volatile hydrocarbon molecules or to loosely bound hydrocarbon precursors, which can be sputtered with much lower threshold energy. Chemical erosion is a complicated multistep process that depends on particle energy and flux, surface temperature, and material properties such as crystalline structure and may be influenced by impurity atoms in the lattice. Modeling and experimental results shown in Refs. 23 and 30 indicate that the chemical sputtering yield peaks at temperatures of ~600 to 700 K and at ion energy levels of ~0.5 keV. Chemical sputtering decreases dramatically at higher temperatures and, thus, should not be of concern for IFE conditions.

Another erosion process observed in ion-beam experiments and unique to carbon is RES, which results in the release of carbon atoms with a thermal velocity distribution.[23,24,30] During ion irradiation, not only surface atoms are displaced from their lattice sites but also atom displacements occur throughout the ion range when energies larger than ~25 eV are transferred in elastic collisions. In graphite, carbon atoms are very mobile between graphitic planes, and atoms that escape recombination with vacancies can reach the surface and evaporate freely. Although RES exists already at room temperature,[23] its yield is smaller than the physical sputtering yield until ~1500 K. At higher temperature, radiation-induced vacancies become mobile, and an increasing number of displaced carbon atoms escape recombination and reach the surface. The erosion yield increases monotonically with surface temperature until above ~2000 K when normal sublimation dominates the erosion. Attempts to reduce RES by doping the carbon material with impurities showed a shift of RES to higher temperature, but in general, no complete suppression has been achieved.[23,24] Figure 15 shows a collection of erosion data illustrating the strong temperature dependence of RES (Ref. 31). The sputtering approaches unity as the temperature

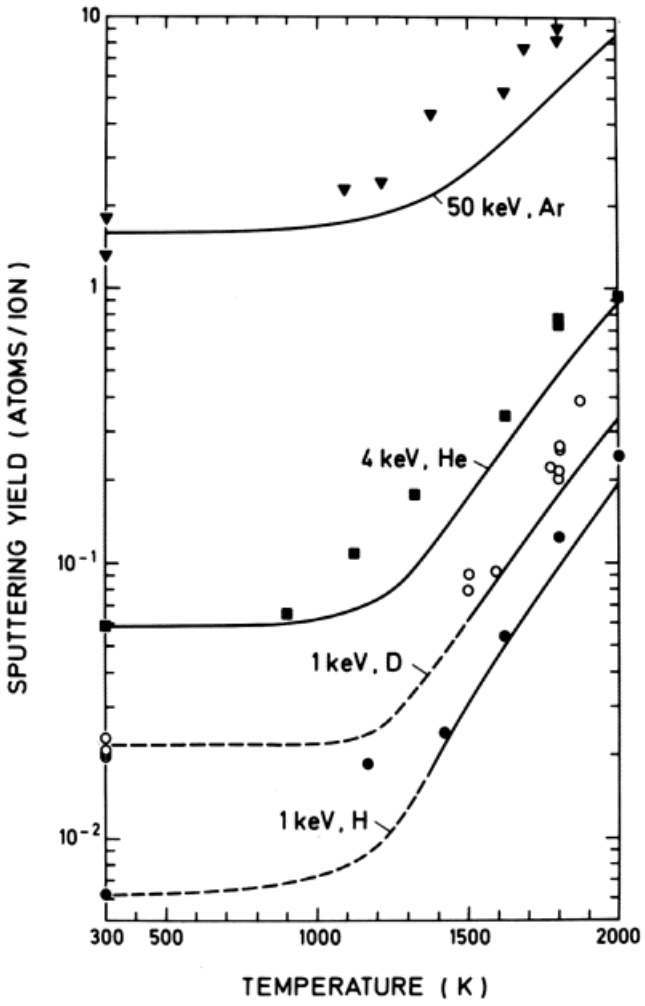

Fig. 15. Temperature dependence of the sputtering yield of pyrolytic graphite by H^+, D^+, He^+, and Ar^+ in the temperature range of RES (reproduced with permission from Ref. 31).

approaches 2000 K in the case of helium ions and, by extrapolation, at temperatures >2000 K for hydrogen and deuterium ions. RES also peaks with ion energies of ~1 keV and decreases appreciably for energies on either side of this.[30]

No data are available for the RES sputtering yield at temperatures higher than ~2000 K (extrapolation from Fig. 15 shows a continuous increase with temperature) and for ion energies higher than ~10 keV (extrapolation from data in Ref. 30 shows a continuous decrease). Thus, it is difficult to make a precise estimate of RES for IFE conditions. If one conservatively assumes a sputtering yield of unity at temperatures >2000 K and ion energies in the range 0.1 to 10 keV, one can make a very rough estimate of RES for the example 154-MJ direct-drive target spectra. The total number of ions of hydrogen and helium species can be calculated as $\sim 4.7 \times 10^{18}$ from the debris ion spectra illustrated in Fig. 4 under the assumption of no protective chamber gas. From Eq. (3), the corresponding annual carbon armor loss due to RES is estimated as ~0.03 mm. Thus, it appears that RES would not play a major role in the IFE armor case. However, there are uncertainties on the sputtering yield values over the full ranges of ion energy and of temperature in the IFE chamber. In addition, the presence of a protective chamber gas would attenuate the ion energies and could result in a larger population of ions at energies between 0.1 to 10 keV and higher RES loss. It seems prudent for carbon armor designers to consider RES when developing the armor design and operating conditions.

VI.B. High-Temperature and Thermal Stress Accommodation

The armor must be able to accommodate the high-energy deposition and related thermal stress without failure over the required lifetime. Of concern are the properties of the armor material at or near the melting or sublimation point. For example, from tests at the RHEPP Ion Source Facility, a certain amount of roughening has been observed in tungsten under cyclic heat loads that seem to occur as the surface deforms to relieve local stresses.[32] One possibility is to design and operate the metallic (tungsten) armor to allow for microsurface melting in order to possibly anneal any defects. In that case, it will be important to understand the dynamics of the melt layer and the possibility of splashing or of flow within the very short time before resolidification. The effect of solidification itself on the tungsten microstructure is also of concern. The tungsten armor could also be designed to operate just below the melting point to avoid melting while providing enough malleability to accommodate local stresses. More data are needed on tungsten armor under IFE-like heat loads to better understand its behavior and help set the desired operating conditions and to find the best microstructure configuration.

In carbon-based material, a phenomenon called "brittle destruction" has been observed in various MFE disruption simulation facilities.[33] It is not clear what are exactly the physical mechanisms that cause this brittle destruction. One possibility could be cracking caused by thermomechanical stresses that develop during the intense deposition of energy. Further studies are under way.

Both melt layer behavior and brittle destruction are being studied as part of the MFE experimental and modeling effort, for example, with models such as HEIGHTS and FOREV-2 (Refs. 34 and 35, respectively). This is another area where synergy between MFE and IFE R&D issues and effort can be very beneficial.

VI.C. Tritium Inventory

Tritium inventory is a major safety issue, and armor-related concerns include tritium implantation and trapping in the bulk of the armor material and, more importantly, in the case of carbon, codeposition with eroded carbon redeposited in cold areas. This has been studied extensively as part of the MFE R&D effort. Reference 23 provides a thorough review of the present understanding in this area, including detailed descriptions of the underlying physical mechanisms for tritium inventory and permeation that provide the basis for models of hydrogen retention and recycling. Here, a brief discussion is provided of some of the key findings in existing tokamaks as they relate to IFE conditions.

Tritium fuel has been successfully used in the Tokamak Fusion Test Reactor (TFTR) and the Joint European Torus (JET), which produce 10 and 16 MW of fusion power, respectively.[36,37] A large fraction of tritium was retained during D-T plasma operations in TFTR and JET by codeposition with eroded carbon and by isotope exchange with previously retained deuterium.[38,39] When the tritium in-vessel inventory approached the administrative safety limit, it was removed by extensive campaigns involving several weeks of glow discharge cleaning and deuterium operation. An unexpectedly large amount of tritium was also transported to the JET subdivertor region. This operation experience pointed clearly to the problem associated with the formation of tritium-rich carbon codeposited layers ($\geq 50\ \mu$m) in cold areas during operations. The retention experience of Alcator C-mod (Ref. 40) is particularly interesting in this respect since it is lined with molybdenum tiles and there are no carbon PFCs. The analysis showed that most of the deuterium inventory was implanted (not codeposited) on the main chamber wall and that the fraction of deuterium retained is drastically lower (~100 times) than in other tokamaks with carbon PFCs.

Operation experience in today's tokamaks points clearly to the fact that MFE devices with carbon PFCs will accumulate tritium by codeposition with the eroded carbon in relatively cold areas, and this will strongly

constrain plasma operations. For example, carbon is currently chosen in ITER to clad the ITER divertor target, near the strike points, because of its greater resilience to excessive heat loads during ELMs and plasma disruptions. However, maintaining carbon in the design has a strong impact on the control of the tritium inventory, and efficient in situ techniques are required to recover the tritium retained in the codeposited layers to avoid frequent interruptions imposed by precautionary operating safety limits or necessitated by fuel economy. Although there are still large uncertainties in estimating the number of plasma pulses that ITER will need to reach the in-vessel mobilizable inventory limit (e.g., $<$500 g of codeposited tritium), there are concerns that this could severely limit plasma operation. Upon reaching that limit, operation would need to be discontinued, and the subsequent availability of the machine for plasma operations would depend on efficient and fast tritium removal techniques that have yet to be fully demonstrated in a tokamak. For comparison, in TFTR, several weeks were needed for tritium removal after only 10 to 15 min of cumulative D-T plasma operation.

Several techniques are being considered for the removal of the tritium-rich codeposited layers. One such technique involves exposure to oxygen (e.g., thermo-oxidative erosion at temperatures $>$570 K, or oxygen plasma discharges) and has been found to be most effective in laboratory experiments to remove tritium from a carbon surface (by removing the tritium-containing films).[41,42] Major drawbacks of such a technique using oxygen, especially at elevated temperatures, include collateral effects on other in-vessel components and recovery time for normal plasma operation. No practical method of localizing the oxidation to the area required (and avoiding oxygen exposure elsewhere) has been developed, although various ideas are being explored. Alternatively, high-temperature baking ($>$1000 K) under vacuum is sufficient to remove the trapped tritium but is technically very difficult to achieve. However, the required removal rate from any technique has not been demonstrated on a tokamak, and this remains a major issue yet to be resolved for next-step devices with carbon PFCs.

For IFE application, carbon redeposition in cold regions (less than $\sim$800 K) can lead to tritium codeposition in the ratio of up to 1:1. This would correspond to $\sim$60 g of tritium for every micron of ablated carbon in a chamber of radius 6.5 m. Although the chamber wall will be at high temperature, there are many penetration lines for the driver where the temperature will be low enough for tritium codeposition to be of concern. As part of R&D activities, techniques must be developed for removal of codeposited tritium through processes such as those outlined above. Based on the current understanding from the MFE situation, solving the carbon codeposition issue is a prerequisite to utilizing carbon as armor material for IFE.

VI.D. Irradiation Effects

Irradiation effects include the effect of neutron irradiation on material properties and mechanical behavior such as the decrease in thermal conductivity[10] and the effect of swelling for carbon under high neutron fluence. It also includes the effect of ion implantation (helium ions in particular) and accumulation in the armor material. For example, in tungsten (in which helium diffusion is very poor), the large fluxes of helium ions can result in a 1 to 1 ratio of tungsten to helium within $\sim$100 days of operation assuming a 1-μm implantation depth. This would lead to failure of chunks of armor and must be remedied by solutions such as operation at high enough temperature for helium to be mobile in tungsten or by using a very fine porous structure (with nanosize being the goal) to provide a very short diffusion path for helium to be transported to open porosity and back to the chamber. The porous structure could also help in accommodating local stresses arising from the high heat fluxes associated with photon and ion energy deposition. These are being investigated as part of the ongoing R&D effort in this area. Other irradiation issues include material activation and the associated disposal and safety concerns that are discussed in Sec. VII.

VI.E. Fabrication

Effort in R&D is needed on the fabrication of the armor material, on its bonding to a structural material, and on the armor and bond integrity under operation. In the case of IFE, particular concerns exist as to the applicability of material (and bonding) properties and behavior developed under equilibrium or moderate transients to the highly cyclic conditions at the armor surface. Fabrication is also an important issue for the development of engineered material such as the fibrous carpet discussed in Sec. V.A and finely structured porous tungsten to enhance helium migration back to the chamber.

Even in the most optimistic case, it is very difficult to guarantee that locally the armor will not erode to an unacceptable level or fail. Thus, it is imperative that in parallel with the R&D effort, methods for in situ repair of the armor be developed to avoid long and costly shutdown for replacement of major wall sections in the event of local failure or erosion.

VII. ACTIVATION ANALYSIS FOR DIRECT-DRIVE AND INDIRECT-DRIVE TARGETS FOR DRY CHAMBER WALL APPLICATION

This section summarizes the key activation issues for the candidate coating/hohlraum materials and examines the influence on the waste management of ARIES-IFE chambers using the radiation conditions of the

dry-wall concept; a more detailed discussion can be found in Ref. 43. Gold and gold/gadolinium have long been considered to be the coating and hohlraum wall materials of choice for the direct-drive and indirect-drive targets, respectively, offering high target performance and low beam energy losses. More recently, a variety of other materials has been considered including tungsten, lead, platinum, palladium, and silver for the direct-drive-target coating and gold, tungsten, lead, mercury, tantalum, cesium, and hafnium for the hohlraum wall of the indirect-drive target.

During burn, the coating/hohlraum debris interact with the source neutrons and become radioactive, then travel through the cavity, and reach the solid wall (assuming a low-density chamber buffer gas) where they are deposited. During the subsequent shots, the condensed materials get reirradiated for several years and then are disposed of with the first wall and blanket at the end of their service lifetime. The accumulation of the radioactive target materials on the first wall has prompted an interest in the issues regarding the waste management of the chamber structure plated with radioactive target debris. The motivation of this assessment is to develop a list of recommended coating/hohlraum materials that would offer outstanding safety features under the assumed operating condition. This would be an important input for target designers and would have to be considered along with other key factors such as target fabrication, performance, and safety issues when developing the target design and composition.

For the example analysis presented here, the radius of the solid first wall was assumed to be 4 m. For the direct-drive-target case, the 154-MJ target served as the in-chamber irradiation source. Consideration of the higher-yield (401-MJ) direct-drive target should not alter the main conclusions from this analysis. The direct-drive spherical shell targets have a radius of 1.95 mm containing the frozen D-T fuel interior layer and are covered with a 300-Å-thick coating. For the indirect-drive target, a 15-μm-thick hohlraum wall, having a volume of 0.0085 cm^3, surrounds the capsule.[44] It is estimated that for a repetition-rate of 6 Hz, approximately 190 million targets per year will be needed. The more massive hohlraums produce much heavy metal debris in the chamber: 20 tonnes/yr of gold/gadolinium as compared with 5 kg/yr for the gold laser coating.

In the spirit of separating the armor function from the first-wall structural function and blanket function, as discussed in Sec. V.A, a tungsten armor has been considered coupled with a first-wall/blanket configuration developed for the ARIES-AT MFE power plant (with SiC_f/SiC as structural material and Pb-17Li as coolant and breeder material).[45] The tungsten armor is assumed to be 2 mm thick and attached to a 10-mm-thick SiC_f/SiC first wall. A graphite armor would offer less radioactivity than tungsten. An assumed burnup limit of 3% for the SiC_f/SiC structure translates into an end-of-life (EOL) fluence of 21 MW·yr/m^2, which means a neutron wall loading of 3.5 MW/m^2 would correspond to a first-wall lifetime of 6 full-power years (FPY). A 44-cm-thick blanket (20% SiC_f/SiC and 80% Pb-17Li, by volume) is sufficient to provide an overall tritium-breeding ratio of 1.1. Over the 6-FPY service lifetime of the first wall, the target materials keep accumulating, reaching a thickness of 8 μm for the laser target coatings and ~5 cm for the more massive indirect-drive hohlraum wall materials. It seems likely that the incident X rays and ions will melt most of the deposited hohlraum materials, and it is assumed that only a deposited layer ~1 mm thick will stick on the wall. The molten materials would run down the first wall, accumulate at the bottom of the chamber, and eventually be removed for disposal or recycling.

The irradiation history for the target coatings and hohlraums was conservatively represented as a pulsed history with a single pulse using the target neutron flux and 10^9 pulses over the 6-FPY period using the lower and softer first-wall flux. Note that the fluence-dependent waste disposal rating (WDR) is insensitive to the first-wall location as long as the material-dependent EOL fluence remains fixed at 21 MW·yr/m^2. This means a larger chamber would call for a lower wall loading and a longer first-wall lifetime and will have a comparable WDR to the 4-m-radius base case. The activity and WDR were computed using the ALARA pulsed activation code[46] and the FENDL-2 175 neutron group transmutation cross-section library. Highly pure materials were assumed for the target materials and tungsten armor. The impurities for the SiC_f/SiC structure are taken from ARIES-AT study. A WDR $\leq$ 1 at the end of a 100-yr institutional control period means the component qualifies as low-level waste for shallow land burial. The WDRs reported herein are based on the Fetter waste disposal limits as they are more restrictive than those of the U.S. Nuclear Regulatory Commission (NRC) for all materials considered in this analysis.

The volume-averaged WDR results are summarized in Tables V and VI for the direct-drive-target coating and indirect-drive holhraum cases, respectively. Two additional cases are also included: coating or hohlraum combined with tungsten armor on a separate first wall and coating or hohlraum combined with tungsten/first wall attached to the blanket. From the design standpoint, it seems desirable to integrate the first wall with the blanket, and in this case, the armor has a relatively small impact on the already low WDR of the SiC first wall/blanket (0.02). This means considerations other than the radiological issues (e.g., evaporation rate by target X rays) will determine the preferred armor material, either tungsten or graphite. The main long-lived radionuclides contributing to the WDR are included between parentheses in Tables V and VI. The reported results are for a fully compacted waste. The main long-lived radionuclides contributing to the WDR of the tungsten armor and SiC_f/SiC structure are ^{186m}Re and ^{26}Al, respectively.

TABLE V

WDR for Target Coating Materials Deposited on the SiC_f/SiC Structure of a Dry-Wall Chamber for a Direct-Drive-Target Case

	Coating Material	Coating/ Tungsten/ First Wall	Coating/ Tungsten/ First Wall/ Boron
	—	0.24	0.04
Gold	0.87 (^{194}Hg)	0.24	0.04
Tungsten	1.03 (^{186m}Re)	0.24	0.04
Lead	3.6 (^{208}Bi)	0.24	0.04
Platinum	169 (^{192n}Ir)	0.35	0.05
Palladium	4.6×10^3 (^{108m}Ag)	3.3	0.4
Silver	1.7×10^5 (^{108m}Ag)	114	12.4

One notes immediately that the gold-plated first wall qualifies as Class-C low-level waste. The silver and gadolinium generate high-level waste (WDR $\gg$ 1) even when the WDR is averaged over the entire first wall/blanket. Of interest is that even a very thin layer of silver or gadolinium on the first wall (1 and 10 μm, respectively) cause waste disposal problems. Admittedly, it is feasible to separate the small amount of ^{108m}Ag and ^{158}Tb radioisotopes from the waste stream and dispose of them as high-level waste. However, the high cost of the isotopic separation process could be prohibitive. If palladium is the preferred coating for laser targets, the palladium-plated first wall and blanket should be disposed of as a single unit to meet the Class-C waste management requirements.

Based on the activation analysis, it is recommended to exclude the silver and gadolinium from the list of candidates and then select the best material(s) based on considerations other than the WDR. Other design issues such as target fabrication/instability/gain, tritium retention and fill time, and off-site doses during an accident may further limit the coating/hohlraum materials choice. The merits and additional cost associated with the exclusion of some materials should be evaluated with the perspective that the incremental change in the cost of electricity is only 5% or less (Ref. 43).

VIII. EXAMPLE SAFETY ANALYSIS FOR DRY CHAMBER WALL

To illustrate the impact of armor selection and performance on the larger safety issue, a scenario leading to a large air ingress into the chamber was considered in the case of a chamber with carbon armor. Such an event may challenge the design to meet the requirements in the U.S. Department of Energy (DOE) Fusion Safety Standard (FSS) (Ref. 47), to avoid public sheltering and evacuation, by keeping off-site doses below 1 rem (10 mSv) in an accident because of the large inventory of tritium in the blanket. This event is also important from an investment protection standpoint since air ingress can lead to oxidation and destruction of the carbon components.

To illustrate the safety analysis, a previously proposed design, the 1000-MW(electric) SOMBRERO design was used for the evaluation. It was assumed that the first-wall and blanket regions of SOMBRERO are constructed of a low-activation carbon/carbon composite material with an assumed 1-kg inventory of trapped tritium.[48] For the present evaluation, in keeping with guidance in the DOE FSS, a severe event was postulated. This scenario consists of a loss-of-flow accident (LOFA) combined with a loss-of-vacuum accident (LOVA) resulting

TABLE VI

WDR for Hohlraum Materials Deposited on the SiC_f/SiC Structure of a Dry-Wall Chamber for an Indirect-Drive-Target Case

	Hohlraum Materials	Hohlraum/ Tungsten/First Wall	Hohlraum/Tungsten/ First Wall/Blanket
	—	0.24	0.04
Gold/gadolinium (50:50)[a]	1.2×10^4 (^{158}Tb)	924	107
Gold	0.87 (^{194}Hg)	0.28	0.043
Lead	3.6 (^{208}Bi)	0.5	0.068
Mercury	0.4 (^{194}Hg)	0.25	0.04
Tantalum	0.06 (^{182}Hf)	0.22	0.04
Tungsten	1.03 (^{186m}Re)	0.3	0.045
Lead/tantalum/cesium (45:20:35)	1.5 (^{208}Bi)	0.34	0.05
Mercury/tungsten/cesium (45:20:35)	0.26 (^{194}Hg, ^{186m}Re)	0.24	0.04
Lead/hafnium (70:30)	2.9 (^{208}Bi)	0.44	0.06

[a]In atom percent.

from a 1-m^2 break in the confinement building. The break in the confinement allows outside air to flow into the chamber, resulting in the oxidation (exothermic reaction) of any exposed high-temperature carbon surfaces. The oxidation rate[49] at the carbon surface is a function of both the temperature of the carbon and the partial pressure of the oxygen in the chamber (see also Ref. 50).

This accident was analyzed recently by two groups of researchers, and the results are reported in Refs. 50 and 51. As an example, the results from Ref. 50 show that the first-wall temperature initially at 1000°C reaches a maximum temperature of ≈1175°C in 2.5 days due to oxidation of the first wall and blanket and then slowly decreases to 800°C by 25 days. Over that period all the tritium in the first wall in the form of HTO (0.78 rem) is assumed released to the environment. This release along with the dose from the xenon gas exceeds the limit offsite dose of 10 mSv (Ref. 48). Our results confirmed that the first-wall temperature initially at 730°C will increase to ≈1100°C, which is slightly lower than the results reported in Ref. 50. The heatup of the first wall is due entirely to the oxidation of the carbon walls (both front and back). The peak temperature is low because of oxygen starvation; i.e., the flow of air through the break is unable to supply enough oxygen to sustain the oxidation rate at a high enough level to generate higher first-wall temperatures; however, both results show that the first wall of the chamber will be completely oxidized. Both results indicate that a better confinement is needed in dry-wall systems to reduce the probability of air ingress into the plasma chamber, thus eliminating the destruction of the first wall and the release of HTO from the carbon walls.

We also looked at a carbon fiber or carbon whisker configuration for the armor, as representative of the fibrous carpet described in Sec. V.A. Our results showed that the heatup and peak first-wall temperature (see Fig. 16) was the same as for the flat carbon wall because the oxidation reaction was limited by oxygen availability (see Fig. 17) even though the surface area for oxidation is increased by a factor of 100. Therefore, there are no obvious detrimental thermal-hydraulic consequences associated with using carbon fibrous carpet armor in place of flat carbon. From a safety perspective, future efforts in dry-wall carbon chambers should focus on improving confinement and/or determine if there is a grade of carbon composite that shows very low reactivity with air and can meet all of the other requirements for use as a chamber first-wall material.

IX. CONCLUSIONS

The IFE chamber wall requirements of integrity, lifetime, and compatibility with reactor operation are quite demanding in view of the challenging cyclic operating conditions both in terms of incident heat fluxes and particle fluxes.

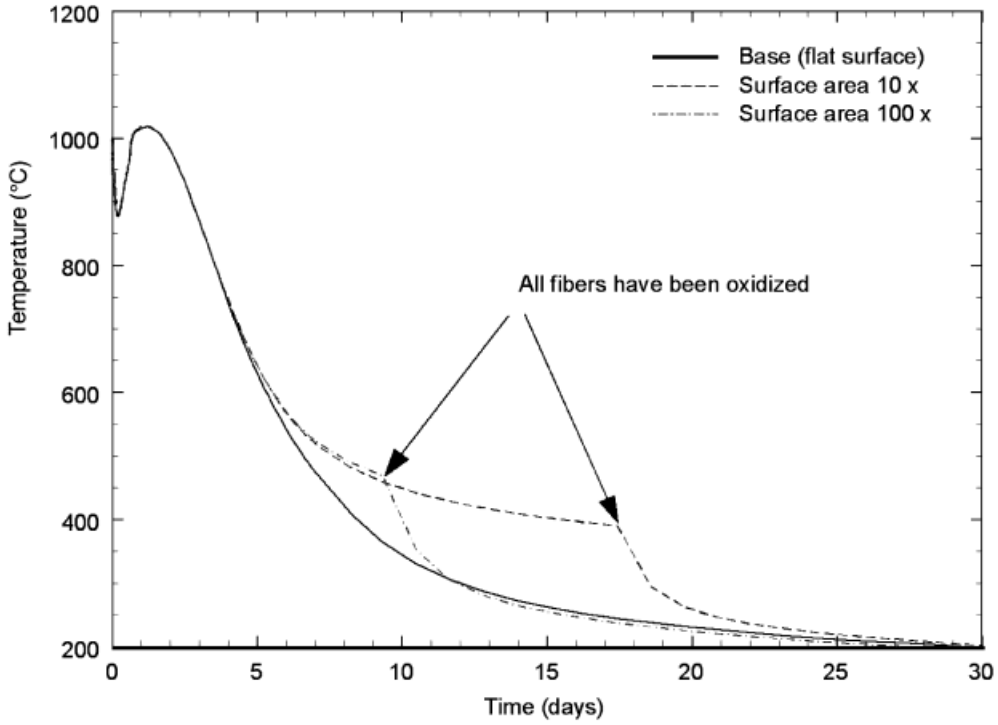

Fig. 16. Surface temperature of carbon armor with different surface areas during LOFA + LOVA accident scenario.

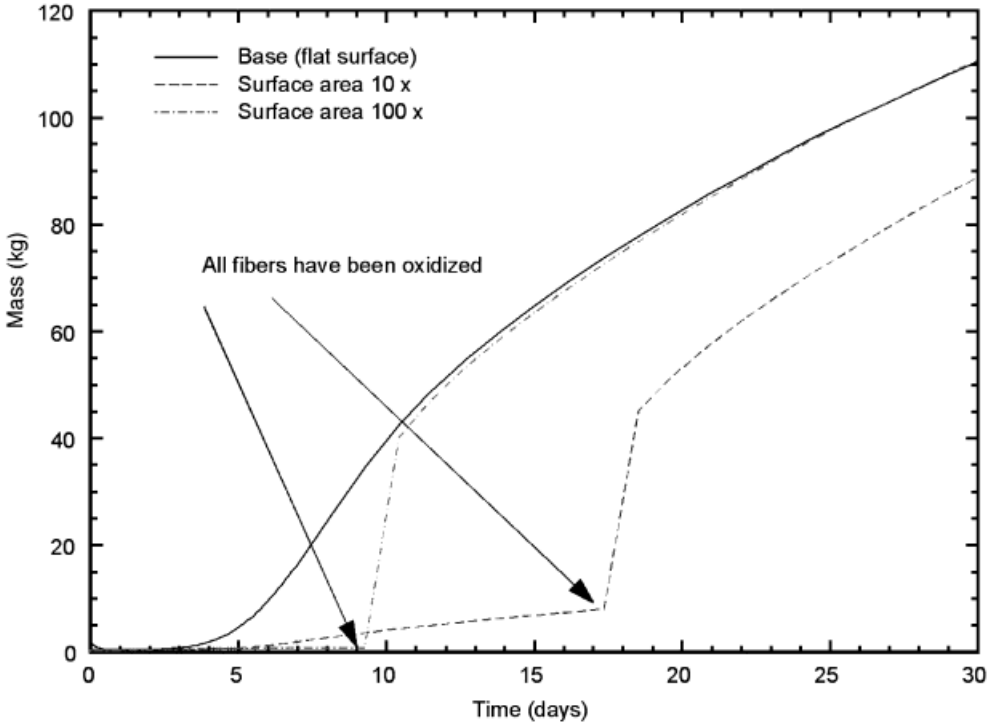

Fig. 17. Mass of oxygen in chamber during LOFA + LOVA accident scenario for carbon armor with different surface areas.

The main dry-wall candidate materials are carbon and refractory metals because of their high temperature capability and their ability to accommodate high heat fluxes. Their use as armor material has been evaluated in the case of direct-drive and indirect-drive targets. In the case of the indirect-drive target, a large fraction of the fusion reaction energy is in the form of X rays, and a high density of protective gas is required for these X rays ($>$200 mtorr in the case of xenon), making it very challenging to accommodate the driver requirements on maximum gas density. A heavy-ion-beam driver with channel transport might be a possibility based on an assumed scattering limit of an integrated line density equivalent to $\sim$1 torr. However, the feasibility and attractiveness of such a combination needs to be further evaluated in the context of a power plant.

For the direct-drive target, a thermal design window exists requiring very low gas density. Calculations show that the threat spectra from the 154-MJ target could be accommodated with some margin by either a carbon or tungsten armor in a 6.5-m (-radius) chamber with a 500°C coolant even in the absence of a protective chamber gas. The presence of a protective gas attenuating the threat to the wall would provide additional flexibility for setting and optimizing the operating conditions, such as the target yield, chamber radius, and coolant temperature parameters for power plant applications. Constraints from target injection and survival as well as from driver requirements would also have to be considered when setting the chamber protective gas density (see Ref. 20).

However, there are some key issues that need to be addressed for both carbon and tungsten armor. For carbon, a major concern for the design, operation, and safety of the system is the erosion of the carbon armor over many pulses, and codeposition of eroded material in combination with tritium, that could result in unacceptably high tritium inventories. For refractory metals, such as tungsten, cyclic operation at high temperature might lead to surface roughening to relieve local stresses. It is speculated that operation near or at the melting point could provide some annealing, but this needs to be verified. Also, with the possibility of melting, concerns about the stability of the melt layer and integrity of the resolidified material over the IFE-relevant timescales must be addressed. The effect of helium ion implantation on the armor integrity is also a key issue in particular for tungsten in which helium diffusion is very slow. The possibility of developing engineered material is being pursued, such as utilizing a finely structured porous tungsten armor to enhance the migration of implanted helium back to the chamber while at the same time providing local stress relief to avoid roughening. High-porosity fibrous materials have also been proposed, such as a fibrous carbon carpet that showed superior ability to accommodate high heat fluxes. However, the carbon erosion and tritium codeposition concerns remain and need to be addressed, for example, by utilizing tungsten or tungsten-coated fibers instead of carbon fibers.

One interesting observation is that although IFE operation is cyclic in nature while MFE operation targets

steady state, there are dynamic MFE operation scenarios (e.g., ELM scenarios) in particular for the next-step device whose loading conditions on the armor show some commonality with IFE. Thus, there is substantial overlap in the configurations and materials considered for MFE and IFE chamber walls and in the related issues. This provides the possibility of synergy between MFE and IFE armor R&D.

With respect to the activation and safety of the chamber, it is recommended to exclude silver and gadolinium from the list of candidate coating/hohlraum materials to avoid deep geological burial of the chamber structure and to design a high-performance confinement system to reduce the probability of air ingress in particular with a carbon-based chamber.

In conclusion, although some major issues still need to be resolved, the analyses show encouraging results for the possibility of utilizing a dry-wall chamber in combination with a laser-driven direct-drive target. A more detailed effort in a power plant context would be required to better determine the attractiveness of such a configuration for power plant application.

ACKNOWLEDGMENTS

This work was supported by the DOE under contract DE-FC03-95ER54299. We would like to acknowledge the help of X. Wang from the University of California, San Diego (UCSD) on the target thermal analysis, M. Zaghloul from UCSD on the energy deposition analysis, D. Henderson and P. Wilson from the University of Wisconsin on the activation analysis, and R. Moore from the Idaho National Engineering and Environmental Laboratory on the safety analysis. We also acknowledge the thoughtful input of C. Skinner from the Princeton Plasma Physics Laboratory on the tritium issues.

REFERENCES

1. I. N. SVIATOSLAVSKY et al., "A KrF Laser Driven Inertial Fusion Reactor 'SOMBRERO,'" *Fusion Technol.*, **21**, 1470 (1992).

2. S. E. BODNER, D. G. COLOMBANT, A. J. SCHMITT, and M. KLAPISCH, "High-Gain Direct-Drive Target Design for Laser Fusion," *Phys. Plasmas*, **7**, *6*, 2298 (2000).

3. D. T. GOODIN, N. B. ALEXANDER, C. R. GIBSON, A. NOBILE, R. W. PETZOLDT, N. P. SIEGEL, and L. THOMSON, "Developing Target Injection and Tracking for Inertial Fusion Energy Power Plants," *Nucl. Fusion*, **41**, 527 (2001).

4. "ARIES-IFE Reference Target Spectra," available on the Internet at ⟨http://aries.ucsd.edu/ARIES/WDOCS/ARIES-IFE/SPECTRA/⟩.

5. D. A. CALLAHAN-MILLER and M. TABAK, "Increasing the Coupling Efficiency in a Heavy Ion, Inertial Confinement Fusion Target," *Nucl. Fusion*, **39**, 1547 (1999).

6. "ESLI" Web site, available on the Internet at ⟨http://www.esli.com⟩, Energy Sciences Laboratory, Inc.

7. P. J. KARDITSAS and M.-J. BAPTISTE, "Thermal and Structural Properties of Fusion Related Materials," available on the Internet at ⟨http://aries.ucsd.edu/LIB/PROPS/PANOS/matintro.html⟩, UKAEA Government Division, Fusion, (Euratom/UKAEA Fusion Association).

8. D. L. SMITH, R. F. MATTAS, and M. C. BILLONE, "Fusion Reactor Materials," *Nuclear Materials*, Part 2, Vol. 10 B, B. R. T. FROST, Ed., Materials Science and Technology, VCH Verlagsgesellschaft mbH, Germany.

9. A. R. RAFFRAY and G. FEDERICI, "RACLETTE: A Model for Evaluating the Thermal Response of Plasma Facing Components to Slow High Power Plasma Transients—Part I: Theory and Description of Model Capabilities," *J. Nucl. Mater.*, **244**, 85 (1997); see also G. FEDERICI and A. R. RAFFRAY, "RACLETTE: A Model for Evaluating the Thermal Response of Plasma Facing Components to Slow High Power Plasma Transients—Part II: Analysis of ITER Plasma Facing Components," *J. Nucl. Mater.*, **244**, 101 (1997).

10. L. L. SNEAD and T. D. BURCHELL, *Carbon Extended Abstracts*, pp. 774–775 (1995).

11. V. PHILIPPS, Personal Communication.

12. "Dr. Eberl MBE-Komponenten GmbH" Web site, available on the Internet at ⟨http://www.mbe-kompo.de/index.html⟩ (2002).

13. "ARIES Properties Archive," available on the Internet at ⟨http://aries.ucsd.edu/LIB/PROPS/PHOTON/⟩.

14. "Particle Interactions with Matter: SRIM—The Stopping and Range of Ions in Matter," available on the Internet at ⟨http://www.srim.org/⟩.

15. R. R. PETERSON et al., The BUCKY and ZEUS-2D Computer Codes for Simulating High Energy Density ICF Plasmas," *Fusion Technol.*, **30**, 783 (1996).

16. T. RENK, Personal Communication; see also T. RENK, "RHEPP Experiments," presented at High Average Power Laser Program Workshop, Washington, D.C., December 5–6, 2002, available on the Internet at ⟨http://aries.ucsd.edu/HAPL/MEETINGS/0212-HAPL/program.html⟩.

17. T. MELHORN, "A Finite Material Temperature Model for Ion Energy Deposition in Ion-Driven Inertial Fusion Targets," *J. Appl. Phys.*, **52**, 6522 (1981).

18. J. MACFARLANE and P. WANG, "Radiative Properties and Line Trapping Effects in Post-Explosion Inertial Fusion Plasmas," *Phys. Fluids B*, **3**, 3494 (1991).

19. D. A. LABUNTSOV and A. P. KRYUKOV, "Analysis of Intensive Evaporation and Condensation," *Int. J. Heat Mass Transfer*, **22**, 989 (1979).

20. F. NAJMABADI, A. R. RAFFRAY, and ARIES TEAM, "Operational Windows for Dry-Wall and Wetted-Wall IFE Chambers," *Fusion Sci. Technol.*, **46**, 401 (2004).

21. A. R. RAFFRAY, G. FEDERICI, A. HASSANEIN, and D. HAYNES, "Dynamic Chamber Armor Behavior in IFE and MFE," *Fusion Eng. Des.*, **63–64**, 597 (2002).

22. J. SETHIAN et al., "Fusion Energy Research with Lasers, Direct Drive Targets, and Dry Wall Chambers," *Nucl. Fusion* (May 2003) (accepted for publication).

23. G. FEDERICI et al., "Plasma-Materials Interactions in Current Tokamaks and Their Implications for Next-Step Fusion Reactors, *Nucl. Fusion*, **41**, 12R (Dec. 2001).

24. P. SIGMUND, "Theory of Sputtering. I. Sputtering Yield of Amorphous and Polycrystalline Targets," *Phys. Rev.*, **184**, 383 (1969).

25. W. ECKSTEIN, C. GARCÍA-ROSALES, J. ROTH, and J. LÁSZLÓ, "Threshold Energy for Sputtering and Its Dependence on Angle of Incidence," *Nucl. Instrum. Methods B*, **83**, 95 (1993).

26. J. ROTH, W. ECKSTEIN, and M. GUSEVA, "Erosion of Be as Plasma-Facing Material," *Fusion Eng. Des.*, **37**, 465 (1997).

27. W. ECKSTEIN, C. GARCÍA-ROSALES, J. ROTH, and W. OTTENBERGER, "Sputtering Data," IPP 9/82, Max-Planck-Institut für Plasmaphysik (1993).

28. W. ECKSTEIN, "Computer Simulation of Ion-Solid Interaction," Springer Series in *Material Science*, Vol. 10, Springer, Berlin (1991).

29. J. BOHDANSKY, H. LINDNER, A. P. MARTINELLI, and J. ROTH, "Sputtering Yield of Cu and Ag at Temperatures Close to the Melting Point," *Nucl. Instrum. Methods B*, **18**, 509 (1987).

30. J. ROTH, E. VIETZKE, and A. A. HAASZ, "Erosion of Graphite due to Particle Impact," *Atomic and Plasma-Material Interaction Data for Fusion*, Vol. 1, supplement to *Nucl. Fusion*, 63 (1991).

31. J. ROTH, "Chemical Sputtering and Radiation Enhanced Sublimation of Carbon," in "Physics of Plasma-Wall Interactions in Controlled Fusion," *NATO ASI Series B: Physics*, p. 389, D. E. POST and R. BEHRISCH, Eds., Plenum Press, New York (1986).

32. T. RENK, Personal Communication (2002).

33. A. HASSANEIN, "Prediction of Material Erosion and Lifetime During Major Plasma Instabilities in Tokamak Devices," *Fusion Eng. Des.* (2002) (accepted for publication).

34. A. HASSANEIN and I. KONKASHBAEV, "Comprehensive Physical Models and Simulation Package for Plasma/Material Interactions During Plasma Instabilities," *J. Nucl. Mater.*, **273**, 326 (1999).

35. H. WUERZ, S. PESTCHANYI, B. BAZYLEV, and F. KAPPLER, "A Consistent 2D Analysis of the ITER 2D Divertor," *Proc. 20th Symp. Fusion Technol.*, Marseille, France, 1998, Vol. 1, p. 271 (1998).

36. A. GIBSON et al., "Deuterium-Tritium Plasmas in the Joint European Torus (JET): Behavior and Implications," *Phys. Plasmas*, **5**, *5*, 1839 (1998).

37. R. J. HAWRYLUK, "Results from Deuterium-Tritium Tokamak Confinement Experiments," *Rev. Modern Phys.*, **70**, 537 (1998).

38. C. H. SKINNER et al., "Studies of Tritiated Co-Deposited Layers in TFTR," *J. Nucl. Mater.*, **290–293**, 486 (2001).

39. P. ANDREW et al., "Tritium Retention and Clean-Up in JET," *Fusion Eng. Des.*, **47**, 233 (1999).

40. W. R. WAMPLER et al., "Long-Term Retention of Deuterium and Tritium in Alcator C-Mod," *Proc. 18th IEEE/NPSS Symp. Fusion Engineering*, p. 267, Institute of Electrical and Electronics Engineers/Nuclear and Plasma Sciences Society (1999).

41. W. WANG, J. ROTH, R. BEHRISCH, and G. STAUDENMAIER, "Material Transport at the Vessel Walls of the Divertor Tokamak ASDEX," *J. Nucl. Mater.*, **162–164**, 422 (1989).

42. J. W. DAVIS and A. A. HAASZ, "Oxygen Removal of Codeposited a-C:D Layers from Tokamak Tiles," *J. Nucl. Mater.*, **266–269**, 478 (1999).

43. L. EL-GUEBALY et al., "Target Activation and Radiological Response of ARIES-IFE Dry Wall Chamber," *Fusion Eng. Des.*, **63–64**, 653 (2002).

44. D. CALLAHAN-MILLER and M. TABAK, "Progress in Physics and Design for Heavy Ion Fusion," *Phys. Plasma*, **7**, *5*, 2083 (May 2000).

45. A. R. RAFFRAY et al. and ARIES TEAM, "High Performance Blanket for ARIES-AT Power Plant," *Fusion Eng. Des.*, **58–59**, 549 (2001).

46. P. WILSON and D. HENDERSON, "ALARA: Analytic and Laplacian Adaptive Radioactivity Analysis Code Technical Manual," UWFDM-1070, University of Wisconsin Fusion Technology Institute (Jan. 1998).

47. "Safety of Magnetic Fusion Facilities: Guidance," DOE-STD-6003-96, U.S. Department of Energy (1996).

48. L. J. WITTENBERG, "A Reinvestigation of the Tritium Inventory in the Carbon Structure of SOMBRERO Direct-Drive ICF Conceptual Design Study," UWFDM-1127, University of Wisconsin Fusion Technology Institute (Mar. 2001).

49. M. H. O'BRIEN, B. J. MERRILL, and S. N. UGAKI, "Combustion Testing and Thermal Modeling of Proposed CIT Graphite Tile Material," EGG-FSP-8255, Idaho National Engineering Laboratory (Sep. 1988).

50. S. REYES, J. F. LATKOWSKI, J. GOMEZ DEL RIO, and J. SANZ, "Accident Doses Analysis of the SOMBRERO Inertial Fusion Energy Power Plant Design," *Fusion Technol.*, **39**, 941 (2000).

51. G. KULCINSKI et al., "The Potential for Graphite Oxidation in Dry Wall ICF Chambers," presented at 2nd Laser IFE Program Workshop, Washington, D.C., May 31–June 1, 2001, available on the Internet at ⟨http://aries.ucsd.edu/LIB/MEETINGS/0105-NRL-LASER-DP/Kulcinski.pdf⟩.